ACS Photonics

pubs.acs.org/journal/apchd5

Letter

Mode-Matching Enhancement of Second-Harmonic Generation with Plasmonic Nanopatch Antennas

Ahsan Noor, Anoop R. Damodaran,* In-Ho Lee, Stefan A. Maier, Sang-Hyun Oh, and Cristian Ciracì*

Cite This: *ACS Photonics* 2020, 7, 3333−3340

Read Online

ACCESS | Metrics & More | Article Recommendations

ABSTRACT: Plasmonic enhancement of nonlinear optical processes confront severe limitations arising from the strong dispersion of metal susceptibilities and small interaction volumes that hamper the realization of desirable phase-matching-like conditions. Maximizing nonlinear interactions in nanoscale systems require simultaneous excitation of resonant modes that spatially and constructively overlap at all wavelengths involved in the process. Here, we present a hybrid rectangular patch antenna design for optimal second-harmonic generation (SHG) that is characterized by a non-centrosymmetric dielectric/ferroelectric material at the plasmonic hot spot. The optimization of the rectangular patch allows for the independent tuning of various modes of resonances that can be used to enhance the SHG process. We explore the angular dependence of SHG in these hybrid structures and highlight conditions necessary for the maximal SHG efficiency. Furthermore, we propose a novel configuration with a periodically poled ferroelectric layer for an orders-of-magnitude enhanced SHG at normal incidence. Such a platform may enable the development of integrated nanoscale light sources and on-chip frequency converters.

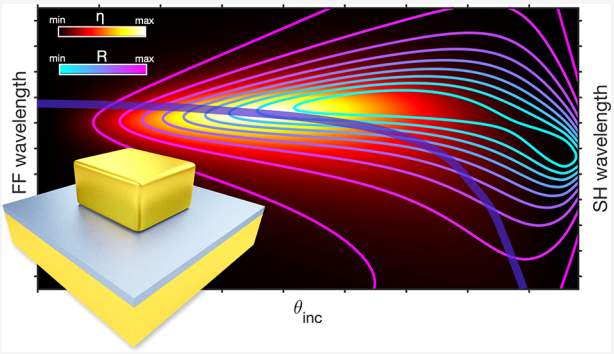

KEYWORDS: *Plasmonics, nonlinear optics, second-harmonic generation, ferroelectrics, hybrid plasmonics, nanopatch antenna*

Optical functionalities achieved through the nonlinear interaction of light with matter are cornerstones of many present-day technological innovations.[1] These include control over the laser spectrum (optical frequency conversion), ultrashort pulse generation, and all-optical signal processing.[2] Optical nonlinear susceptibilities of natural materials are intrinsically low, and conventional nonlinear optical devices rely on high laser intensities and long propagation distances in macroscopic crystals in order to exhibit sizable nonlinear effects.[2] Such devices are often not compatible with an integrated design and, consequently, hinder the realization of efficient nanoscale nonlinear optical components, which are essential for all-optical signal processing in photonic integrated circuits. To this end, the resonant excitation (electromagnetic field enhancements) of nonlinear dielectric-based nanoresonators,[3−7] plasmonic metamaterials,[8−20] and hybrid metal-dielectric metamaterials/metasurfaces and waveguides[21−33] has been proposed to improve the efficiency of nonlinear optical processes in small volumes. Among the nonlinear optical processes, achieving efficient frequency conversion at the nanoscale is particularly desirable for many applications in biosensing,[34] photonic circuitry,[29] and quantum optics.[35] The difficulty in realizing efficient frequency conversion at the nanoscale arises from the fact that some of the factors that contribute to the wave-mixing processes are often hard to satisfy simultaneously. In particular, a nanosystem needs to fulfill three main requirements:[30,36] (i) generate local field enhancement, through the excitation of resonant modes, at all the wavelengths involved in the nonlinear process;[36−39] (ii) the different modes at the frequencies of interest need to exhibit significant spatial overlap in order to maximize their interaction in the nonlinear volume;[30,31] and (iii) nonlinear polarization currents need to constructively add up and efficiently couple to the far field.[40] A nanosystem that fulfills all the aforementioned properties and simultaneously offers the possibility of realizing an experimentally viable design may pave the way toward the realization of the efficient nanoscale nonlinear devices.

Plasmonic structures can be used for nonlinear optics in two distinct configurations:[41,42] (i) a pure nonlinear-plasmonic configuration, in which the intrinsic nonlinear responses of the metals in the system are exploited,[9−11,36,39,43−46] and (ii) a hybrid plasmonic-dielectric configuration, where plasmonic enhancement is used to enhance the nonlinear responses of

Received: October 5, 2020
Published: November 25, 2020

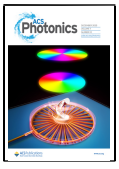

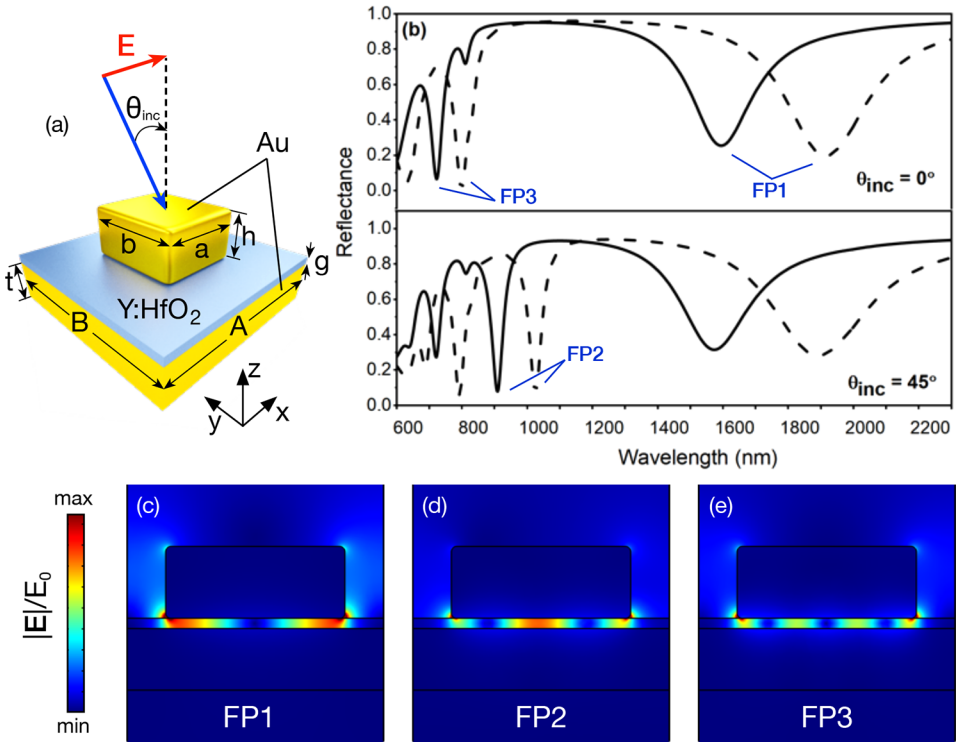

Figure 1. Device layout and its linear electromagnetic response. (a) Schematic of the unit cell of film-coupled nanopatch system and an illustration of its design parameters. (b) Simulated linear reflectance spectra for different values of the patch width *a* (the dashed lines shows the spectra obtained by 20% increase in *a*); (c–e) the normalized electric-field distributions (in the *xz* plane) of the modes indicated as FP1, FP2, and FP3 in (b).

optically active dielectric materials.[15−17,21,25] Although metals may possess large second- and third-order nonlinear susceptibilities, their opaqueness makes the design of pure nonlinear-plasmonic configurations challenging. Moreover, second-order nonlinear processes require a break of symmetry both at the microscopic level (i.e., at the metal surface) and at the macroscopic level (structure asymmetry) to avoid near- and far-field cancellation. This condition is difficult to achieve in some of the most efficient plasmonic systems, often characterized by locally symmetric gaps. This includes the case of two nanoparticles a few nanometers apart (in a dimer configuration) that are known to demonstrate some of the largest local field enhancements.[47,48] Likewise, plasmonic systems formed by metallic nanoparticles over a metallic film, such as film-coupled nanosphere[49−51] and nanopatch antennas,[52,53] retain the characteristics of a dimer configuration in terms of local field enhancements, while simultaneously offering a more precise control over the thickness of gaps using modern fabrication techniques such as layer-by-layer deposition[50,51] and atomic layer deposition (ALD).[54] Compared to its film-coupled nanosphere counterpart, plasmonic film-coupled nanopatch systems possess a richer mode structure. Film-coupled nanopatch systems support *gap-plasmon* modes that are induced between the flat face of the nanopatch antenna and the metallic film.[19,55] The unique properties of these modes include a wider range of tunability of resonances through a careful selection of various design parameters of the system (e.g., the size of the nanopatch or the gap between the film and patch) and an efficient far-field coupling due to the magnetic-dipole-like emission pattern of the patch antenna system.[56−59] Encompassing a robust resonant response,[55] efficient free-space coupling,[57,58] and relative ease of fabrication and incorporation of optically active dielectric gap materials, the nanopatch antenna system is an ideal candidate for developing efficient on-chip nonlinear devices.

To bolster the efficiency of the nonlinear processes involving plasmonic components, often a single resonance is matched either with the fundamental wavelength to enhance the pump intensities[9,11,32] or with the generated harmonic wavelength[60] to enhance the emission efficiency. This approach has been employed to demonstrate enhanced third-order nonlinear optical processes in film-coupled nanopatch antennas[15,17,61] and its two-dimensional counterpart, that is, film-coupled nanowires,[16,32,62] with plasmonic resonances tuned at the pump wavelengths. Other nanoantenna designs have been proposed to realize doubly- or multiresonant designs for second-harmonic generation (SHG) and sum- and difference-frequency generation.[36,39,63] Recently, nanopatch antennas have been exploited to demonstrate enhanced SHG through coupling between the gap-plasmon mode of the nanopatch system and the epsilon-near-zero mode of the spacer layer,[19] and simultaneous control of third-harmonic generation, sum-frequency generation, and four-wave mixing.[33] Doubly resonant colloidal nanocube antennas have also been proposed to enhance SHG.[64] In this case, however, the lack of independent control of the patch dimensions makes it very difficult to doubly match the system's resonances, giving rise to a poor spatial mode overlap and incoherent SHG signals.

In this article, we present a numerical investigation of mode-matched SHG from plasmonic nanopatch antennas that overcome previous limitations. The proposed system operates in the hybrid framework, with a thin dielectric spacing layer of a non-centrosymmetric material acting as the source of nonlinearity within a plasmonic structure. First, characteristics

https://dx.doi.org/10.1021/acsphotonics.0c01545
ACS Photonics 2020, 7, 3333−3340

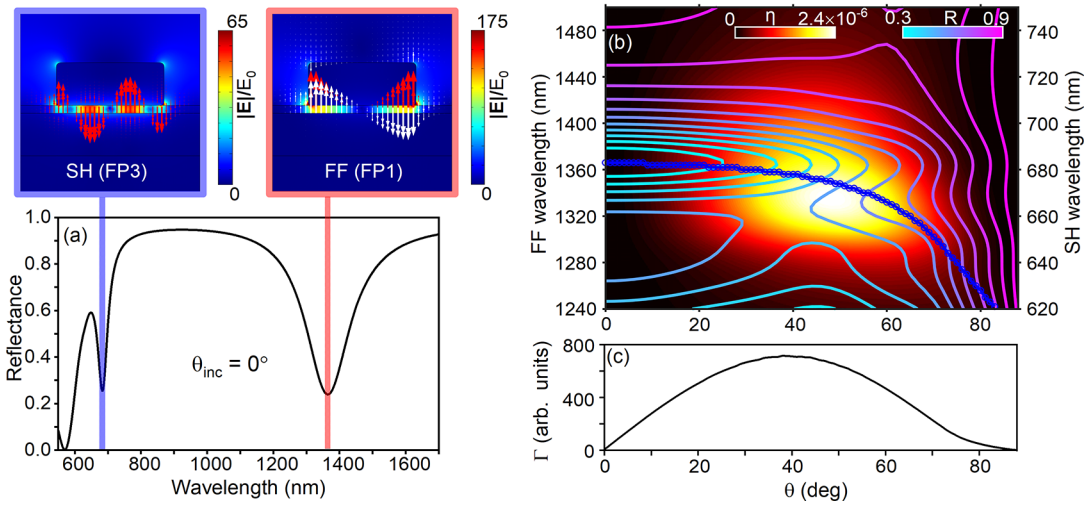

Figure 2. Mode-matched design optimized for the interaction of mode FP1 and mode FP3. (a) The linear response: the reflectance spectra and normalized electric field distributions (in the *xz* plane) of modes at the interacting wavelengths; the insets show the electric-field distribution maps in the *xz* plane; red and white arrows indicate the E_z and the E_z^2 components, respectively. (b, c) The nonlinear response of the system: (b) the SHG efficiency (heat map), linear reflection around the SHG wavelength (contour lines), and the FP1 trajectory (blue curve) as a function of the incident angles and wavelengths and (c) the overlap integral extracted following the blue trajectory in (b). The geometrical parameters are a = 150 nm, b = 80 nm, g = 11 nm, h = 60 nm, t = 60 nm, A = 250 nm, and B = 200 nm (refer to the schematic of the unit cell in Figure 1a).

of the linear response of the plasmonic system and the modes taking part in mode-matched SHG are discussed. The linear resonant characteristics of two optimized mode-matched configurations of distinct modal interactions and their SHG efficiency spectra are then introduced and analyzed. We show how the symmetry of the modes taking part in the nonlinear process might lead to a higher or lower SHG efficiency and associate this behavior to the maximization/minimization of the *overlap integral*, a key parameter in a nonlinear emission process. Finally, we present an ideal system that maximizes the SHG efficiency through the optimization of this integral.

As already stated, the nanopatch antenna system offers a variety of resonant modes that can be used to enhance nonlinear interactions. The wavelengths associated with these modes can be tuned by acting on the geometrical parameters of the system. In particular, we consider a periodic array whose unit-cell design consist of a rectangular gold patch coupled to a gold substrate through a dielectric layer, as illustrated in Figure 1a. We consider a HfO_2-based ferroelectric spacer that can be grown using mature ALD processes with excellent complementary metal-oxide-semiconductor (CMOS) compatibility and potential for on-chip integration.[65,66]

We perform numerical calculations using a commercial software based on the finite-element method and incorporate in our simulations the dispersive dielectric permittivity of gold,[67] a complex dielectric constant n = 1.955 + 0.0045i, and an effective second-order nonlinear optical coefficient $\chi^{(2)}$ of 6 pm/V for the HfO_2-based ferroelectric material embedded in the gap (in the wavelength range considered here (from 0.6 to 2.4 μm) the refractive index is almost a constant).[32]

Figure 1b (top) shows a typical spectrum of the patch antenna system for a transverse magnetic (TM) polarized plane wave at normal incidence. The system exhibits two resonances (indicated as FP1 and FP3; as we will show later, these resonances correspond to Fabry-Pérot modes of the first and third order associated with the gap plasmons) that are ideal candidates to achieve mode matching for the SHG processes. In general, however, because of the dispersion of metallic permittivities, it is very difficult for these resonances to satisfy the energy conservation condition, that is, $\omega_{FP3} = 2\omega_{FP1}$. A rectangular patch, however, allows to overcome this limitation. By acting on the dimensions of the patch aligned along the x and y directions separately, it is in fact possible to tune almost independently the two resonances. For example, by increasing the arm length a (see the dashed curve in Figure 1b), it is possible to largely shift the mode FP1, while only slightly modifying the mode FP3.

For oblique illumination, a distinct resonance indicated by FP2 in Figure 1b (bottom) is excited. The tuning characteristics of this mode are similar to those of modes FP1 and FP3. The spatial configuration however is different among all the excited modes, as can be observed from the normalized electric field maps presented in Figure 1c–e. The electric field distributions of the modes FP1 and FP3 (for normal and oblique incidence) and FP2 (excited under oblique illumination) can be associated with Fabry-Pérot modes of the first, third, and second orders, respectively. In what follows, we will realize two optimized designs for SHG, with mode matching achieved through the interaction of the mode FP1 with either mode FP2 or FP3.

It is worth mentioning that, in general, all the geometrical parameters such as thickness of the dielectric spacer and the lattice constant of the unit-cell contribute to tuning the resonance positions. The choice of these parameters allows also for controlling the device operating spectral range.

In Figure 2, we show the electromagnetic response of the mode-matched design optimized for the interaction of modes FP1 and FP3. The design is optimized for a nonlinear conversion of infrared incident to a visible light, as apparent from its linear reflection spectra presented in Figure 2a (the optimized design parameters are detailed in the figure caption). The choice of these two modes is driven by three main factors: (i) they can be easily excited at normal incidence, (ii) the energy-matching condition can be realized while keeping reasonable values of the geometrical parameters, and (iii) there is a clear overlap between the two modes. For these reasons,

https://dx.doi.org/10.1021/acsphotonics.0c01545
ACS Photonics 2020, 7, 3333–3340

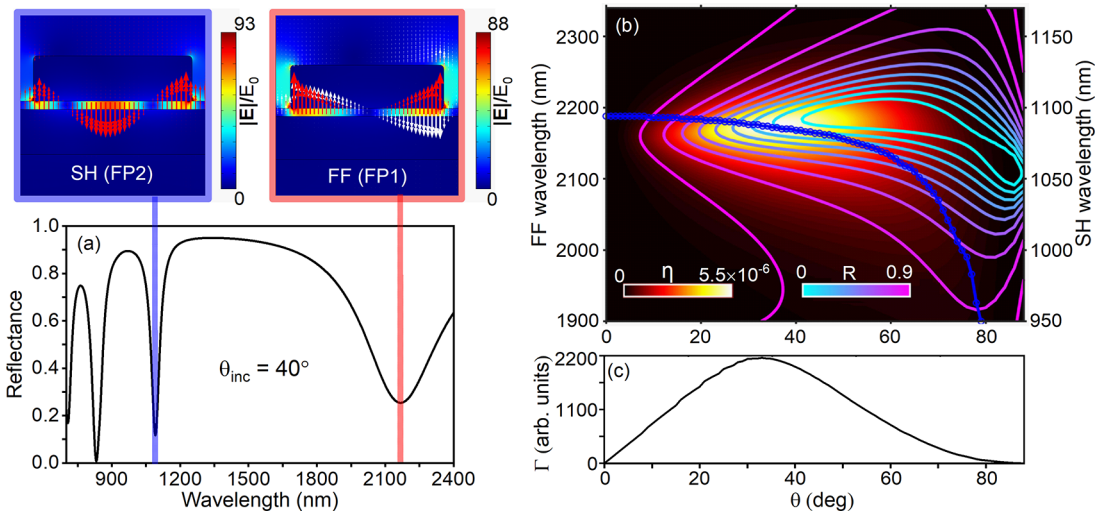

Figure 3. Mode-matched configuration optimized for the interaction of modes FP1 and FP2. (a) The linear reflectance spectra at an incident angle of $\theta = 40°$ with the normalized electric-field distributions at the resonant wavelengths; the insets show the electric-field distribution maps in the xz plane; red and white arrows indicate the E_z and the E_z^2 components, respectively. (b, c) The nonlinear response: (b) second-harmonic efficiency spectra (heat-map, linear reflection around the SHG wavelength (contour lines), and the FP1 trajectory (blue curve) as a function of the incident angles and wavelengths and (c) the overlap integral extracted following the blue trajectory in (b). The geometrical parameters are the same as in Figure 2 with a = 211 nm and b = 170 nm.

one would expect this system to generate the largest SHG conversion, but as we will show there is one more very important factor that one needs to consider.

To numerically evaluate the efficiency of the system, we perform SHG calculations assuming the undepleted pump approximation using a one-way-coupled system of two equations (as detailed in the Methods section). The conversion efficiency η (see eq 3 in the Methods section) is evaluated for a TM-incident field carrying an intensity of $I_{FF} \simeq 55$ MW/cm^2, impinging at different angles and wavelengths. The summary of SHG calculations for the optimized system is shown in Figure 2b. The SHG efficiency map as a function of the incident angle and wavelength is overlapped to the FP1 linear trajectory (blue curve) and linear reflection contour map around the second-harmonic (SH) wavelength.

The system exhibits a modest conversion efficiency on the order of $\eta \simeq 1.2 \times 10^{-9}$ at normal incidence, where there is a perfect overlap of the modes FP1 and FP3 at the fundamental and second-harmonic wavelengths, respectively (see Figure 2b). For oblique illuminations, however, a gradual increase in the conversion efficiency is observed, with a maximum value reaching 3 orders of magnitude higher than the efficiency recorded under normal incidence, $\eta \simeq 2.4 \times 10^{-6}$, at an incidence angle of ~45°. Note that this maximum in the conversion efficiency does not seem to correspond to any particularly favorable spectral condition.

To understand this behavior it is useful to introduce the *overlap integral* defined as[3]

$$\Gamma = \left| \int_{\Omega} \chi^{(2)} \vdots \mathbf{E}(\omega)\mathbf{E}(\omega)\mathbf{E}(2\omega)^* \, d\Omega \right| \quad (1)$$

where $\chi^{(2)}$ is the second-order nonlinear susceptibility tensor, while $\mathbf{E}(\omega)$ and $\mathbf{E}(2\omega)$ are the linear local fields at the fundamental and second-harmonic wavelengths, respectively. The integral is performed over the nonlinear volume Ω. The overlap integral Γ represents the *propensity* of the energy to flow from the fundamental to the second-harmonic mode. From its definition, it is clear that, in order to maximize Γ in Equation 1, local field enhancements at the wavelengths of interaction and spatial overlap are not sufficient. The product of the fields in the integrand needs to add up constructively, that is, the modes must have the correct symmetry. It is interesting to remark that, for plane waves, Γ is maximized when the phase-matching condition ($k_{2\omega} = 2k_{\omega}$) is satisfied.

To easily visualize how the fields interact, note that, in the film-coupled nanopatch systems, resonant local electric fields in the gap are predominantly polarized perpendicularly to the surface of the metal, that is, $\mathbf{E} \simeq (0, 0, E_z)$. In Figure 2a, the normalized electric field distribution map of the mode excited at the fundamental field (FF) wavelength, labeled as FF (FP1), reports its z-component $E_z(\omega)$ with white arrows, while red arrows refer to its squared values, $E_z^2(\omega)$. Similarly, the red arrows in the field-distribution map of the mode excited at second-harmonic wavelength, indicated as SH (FP3), correspond to its z-component, $E_z(2\omega)$. It is easy to see how an antisymmetric mode at the second-harmonic wavelength interacting with the square of an antisymmetric mode at the fundamental wavelength (red arrows in both the field distribution maps) will minimize Γ, instead of maximizing it. This can be also observed in the overlap integral shown in Figure 2c, calculated along the trajectory of FP1. The lowest magnitude of the overlap integral is observed at normal incidence, which leads to a smaller conversion efficiency despite the field enhancements at the wavelengths of interaction. For oblique illumination, however, a break in the symmetry results in the increase of the overlap integral and a gradual increase (peaking in the range of 40−50°), as can be observed in the SHG efficiency spectra in Figure 2b.

To avoid the cancellation effects due to the antisymmetric nature of the mode FP3, let us now consider the interaction of the mode FP1 with the mode FP2. The symmetric nature of the mode FP2 should in fact ensure the maximum efficiency conversion. The linear characteristics of the mode-matched design optimized for such an interaction are shown in Figure 3a, for a TM-polarized excitation impinging at $\theta = 40°$.

https://dx.doi.org/10.1021/acsphotonics.0c01545
ACS Photonics 2020, 7, 3333−3340

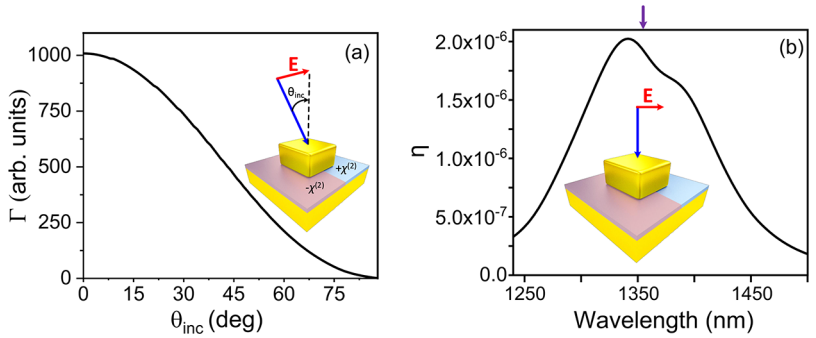

Figure 4. (a) The overlap integral along the FP1 trajectory in Figure 2b for the poled system depicted in the inset; (b) SHG efficiency spectra at normal incidence; the purple arrow indicates the FP1 spectral position at $\lambda_{FP1} = 2\lambda_{FP3} = 1366$ nm.

This design is optimized to operate in the infrared regime. Figure 3b shows the SHG efficiency map as a function of the incident angle and wavelength. The FP1 linear trajectory (blue curve) and linear reflection contour map around the second-harmonic wavelength are layered on top. In this case, the lowest values of SHG efficiency at normal incidence are expected, since the FP2 mode cannot be excited (see the contour levels in Figure 3b). For oblique illumination, the system exhibits a gradual increase in the SHG efficiency with a peak value of 5.5×10^{-6} at $\theta \simeq 35°$. The peak SHG efficiency for this mode-matched design is increased twofold in comparison with the peak efficiency of the previous design. For completeness, we also show in Figure 3c the value of the overlap integral Γ along the FP1 trajectory in Figure 3b. Similarly to the previous case, Γ follows qualitatively the SHG efficiency trend. Note however that differences between peak angles could be due to the out-coupling efficiency of the mode, which is not considered in the overlap integral calculation.

Both configurations analyzed so far require to excite the patch antenna system at an oblique incidence, to achieve maximum possible SHG efficiencies. Ideally, one could remove this inconvenience by using a periodically poled ferroelectric spacer, such that half of the patch would lay over a $-\chi^{(2)}$ material while the other half on a $+\chi^{(2)}$ material, as shown in the inset of Figure 4a.

In such a configuration, one would be able to optimize the overlap integral between the FP1 and FP3 modes at normal incidence by breaking the symmetry through the sign of $\chi^{(2)}$. This is shown in Figure 4a, where Γ is calculated over the FP1 trajectory shown in Figure 2b. This time the maximum magnitude of the overlap integral is obtained at $\theta = 0°$, where quasi-phase-matching between the modes involved is obtained. In Figure 4b, we show the SHG efficiency for a poled patch antenna system at normal incidence for an interval of frequencies around the modes FP1 and FP3 for the fundamental and second-harmonic wavelength, respectively. As expected, in this case, the conversion is much more efficient ($\eta \simeq 2.0 \times 10^{-6}$) than in the previous case (see Figure 2b) at normal incidence. Interestingly, however, the overall maximum value of η remains very close to the maximum value in the previous case.

In conclusion, we have presented a strategy to doubly mode-match plasmonic resonances for efficient SHG using nanopatch antennas in the visible and near-infrared regimes. We have numerically explored different configurations by providing optimized designs for mode-matching of different types of resonances. Our study has shown that a doubly resonant structure with spatial mode overlap does not guarantee maximum efficiency. In fact, a destructive interference of the generated fields may lead to a weak harmonic conversion. This can be overcome by exciting the system at a nonzero angle of incidence. In general, a measure of propensity of two modes to constructively interact can be obtained by calculating the overlap integral Γ, defined in Equation 1. In all our calculations, Γ describes very well the trend of the nonlinear SHG efficiency. Finally, we have shown that efficient SHG at normal incidence can be obtained using a periodically poled ferroelectric spacer,[65,66] by correctly aligning the poling periodicity with the patch patterning.

The obtained efficiencies are comparable (for analogous input powers) to those obtained with dielectric AlGaAs nanoantennas,[5] whose nonlinear susceptibility is 2 orders of magnitude larger than the value considered in this article. This work shows the great potential and versatility of plasmonic nanopatach antennas for nonlinear nanophotonic applications.

METHODS

The SHG process can be described in the frequency domain, under the undepleted pump approximation, by the following set of equations:[2]

$$\nabla \times \nabla \times \mathbf{E}_1(\mathbf{r}) - k_1^2 \epsilon(\mathbf{r}, \omega)\mathbf{E}_1(\mathbf{r}) = 0 \tag{2a}$$

$$\nabla \times \nabla \times \mathbf{E}_2(\mathbf{r}) - k_2^2 \epsilon(\mathbf{r}, 2\omega)\mathbf{E}_2(\mathbf{r}) = 4\mu_0 \omega^2 \mathbf{P}^{(\mathrm{NL})}(\mathbf{r}) \tag{2b}$$

where $k_1 = \omega/c$, $k_2 = 2\omega/c$, with ω being the fundamental field's angular frequency; $\epsilon(\mathbf{r}, \omega)$ is the dispersive permittivity representing the different materials of the design, μ_0 is the permeability of free space, and c is the speed of light in vacuum. In the above system of equations, Equation 2a describes the electric field at the fundamental frequency $\mathbf{E}_1$, whereas Equation 2b is an inhomogeneous vector wave equation that is solved for the generated (second-harmonic) signal $\mathbf{E}_2$. The right-hand side of Equation 2b represents the contributions from nonlinear sources in the system. For simplicity we considered a nonlinear polarization vector possessing the z-component only. This is justified by the following reasons. First, the main components of the electric field of the modes excited in the film-coupled nanopatch system, as discussed in the main text, are primarily polarized perpendicular to the metallic surface (i.e., along the z-direction). Second, the dominant component of the second-order susceptibility tensor exhibited by the nonlinear dielectric material filling the gap between the metallic nanopatch and the film is $\chi^{(2)}_{zzz}$, whose orientation can be controlled through the

https://dx.doi.org/10.1021/acsphotonics.0c01545
ACS Photonics 2020, 7, 3333−3340

film growth.[66] We defined then the nonlinear polarization vector as $\mathbf{P}^{(NL)} = (0, 0, \epsilon_0 \chi^{(2)}_{zzz} {E_{1,z}}^2)$, with $\chi^{(2)}_{zzz} = 6\text{pm/V}$. Note that $\mathbf{P}^{(NL)} \neq 0$ only in the thin film embedded in the gap between the metallic film and the nanopatch.

Equation 2a and Equation 2b are numerically solved using the finite-element method (FEM) within a customized frequency-dependent implementation. Solving eqs (2) is a two-step process:[11,32] first, we solve Equation 2a under TM-polarized incidence for the fundamental field $\mathbf{E}_1$; in the subsequent step, the second harmonic signal is extracted by solving Equation 2b, with the nonlinear polarization term, which is defined by utilizing the fields calculated in the first step. The equations are solved using periodic boundary conditions, to mimic the electromagnetic response of an infinitely extended periodic array.

The nonlinear conversion efficiency η is defined as[11]

$$\eta = \frac{I_{SHG}}{I_{FF}} \tag{3}$$

where I_{FF} is the incident intensity at the fundamental wavelength ω, and I_{SHG} is the intensity of a generated signal measured in the far field, along the specular direction with respect to the incident excitation. The intensity of the incident fields considered in the simulations is $I_{FF} \simeq 55\ \text{MW/cm}^2$. To avoid possible numerical artifacts due to the field localization near the metal corners, we considered a rounded corner cube with a radius of curvature of 5 nm.

AUTHOR INFORMATION

Corresponding Authors

Anoop R. Damodaran − *Department of Electrical and Computer Engineering, University of Minnesota, Minneapolis 55455, Minnesota, United States*; Email: rdanoop@umn.edu

Cristian Ciracì − *Center for Biomolecular Nanotechnologies, Istituto Italiano di Tecnologia, Arnesano 73010, Italy*; orcid.org/0000-0003-3349-8389; Email: cristian.ciraci@iit.it

Authors

Ahsan Noor − *Center for Biomolecular Nanotechnologies, Istituto Italiano di Tecnologia, Arnesano 73010, Italy; Dipartimento di Ingegneria Elettrica e dell'Informazione, Politecnico di Bari, Bari 70125, Italy*

In-Ho Lee − *Department of Electrical and Computer Engineering, University of Minnesota, Minneapolis 55455, Minnesota, United States*

Stefan A. Maier − *Chair in Hybrid Nanosystems, Nanoinstitut Munich, Faculty of Physics, Ludwig-Maximilians Universität München, München 80539, Germany; Experimental Solid State Physics Group, Department of Physics, Imperial College London, London SW7 2AZ, UK*

Sang-Hyun Oh − *Department of Electrical and Computer Engineering, University of Minnesota, Minneapolis 55455, Minnesota, United States*; orcid.org/0000-0002-6992-5007

Complete contact information is available at: https://pubs.acs.org/10.1021/acsphotonics.0c01545

Notes

The authors declare no competing financial interest.

ACKNOWLEDGMENTS

I.-H.L. and S.-H.O. acknowledge support from the National Science Foundation (NSF ECCS 1809723 and ECCS 1809240) and the Sanford P. Bordeau Chair in Electrical Engineering at the University of Minnesota. S.A.M. acknowledges the Deutsche Forschungsgemeinschaft (Germany's Excellence Strategy EXC 2089/1−390776260 e-conversion), the Engineering and Physical Sciences Research Council (EP/M013812/1), and the Lee-Lucas Chair in Physics. A.R.D. acknowledges support from the Regents of the University of Minnesota.

REFERENCES

(1) Garmire, E. Nonlinear optics in daily life. *Opt. Express* **2013**, *21*, 30532−30544.

(2) Boyd, R. W. *Nonlinear Optics*; Elsevier, 2008.

(3) Carletti, L.; Locatelli, A.; Stepanenko, O.; Leo, G.; De Angelis, C. Enhanced second-harmonic generation from magnetic resonance in AlGaAs nanoantennas. *Opt. Express* **2015**, *23*, 26544−26550.

(4) Liu, S.; Sinclair, M. B.; Saravi, S.; Keeler, G. A.; Yang, Y.; Reno, J.; Peake, G. M.; Setzpfandt, F.; Staude, I.; Pertsch, T.; Brener, I. Resonantly enhanced second-harmonic generation using III−V semiconductor all-dielectric metasurfaces. *Nano Lett.* **2016**, *16*, 5426−5432.

(5) Gili, V. F.; Carletti, L.; Locatelli, A.; Rocco, D.; Finazzi, M.; Ghirardini, L.; Favero, I.; Gomez, C.; Lemaître, A.; Celebrano, M.; De Angelis, C.; Leo, G. Monolithic AlGaAs second-harmonic nanoantennas. *Opt. Express* **2016**, *24*, 15965−15971.

(6) Sautter, J. D.; Xu, L.; Miroshnichenko, A. E.; Lysevych, M.; Volkovskaya, I.; Smirnova, D. A.; Camacho-Morales, R.; Zangeneh Kamali, K.; Karouta, F.; Vora, K.; Tan, H. H.; Kauranen, M.; Staude, I.; Jagadish, C.; Neshev, D. N.; Rahmani, M. Tailoring second-harmonic emission from (111)-GaAs nanoantennas. *Nano Lett.* **2019**, *19*, 3905−3911.

(7) Koshelev, K.; Kruk, S.; Melik-Gaykazyan, E.; Choi, J.-H.; Bogdanov, A.; Park, H.-G.; Kivshar, Y. Subwavelength dielectric resonators for nonlinear nanophotonics. *Science* **2020**, *367*, 288−292.

(8) Bouhelier, A.; Beversluis, M.; Hartschuh, A.; Novotny, L. Near-field second-harmonic generation induced by local field enhancement. *Phys. Rev. Lett.* **2003**, *90*, 013903.

(9) Klein, M. W.; Enkrich, C.; Wegener, M.; Linden, S. Second-harmonic generation from magnetic metamaterials. *Science* **2006**, *313*, 502−504.

(10) Canfield, B. K.; Husu, H.; Laukkanen, J.; Bai, B.; Kuittinen, M.; Turunen, J.; Kauranen, M. Local field asymmetry drives second-harmonic generation in noncentrosymmetric nanodimers. *Nano Lett.* **2007**, *7*, 1251−1255.

(11) Zeng, Y.; Hoyer, W.; Liu, J.; Koch, S. W.; Moloney, J. V. Classical theory for second-harmonic generation from metallic nanoparticles. *Phys. Rev. B: Condens. Matter Mater. Phys.* **2009**, *79*, 235109.

(12) Ko, K. D.; Kumar, A.; Fung, K. H.; Ambekar, R.; Liu, G. L.; Fang, N. X.; Toussaint, K. C., Jr Nonlinear optical response from arrays of Au bowtie nanoantennas. *Nano Lett.* **2011**, *11*, 61−65.

(13) Harutyunyan, H.; Volpe, G.; Quidant, R.; Novotny, L. Enhancing the nonlinear optical response using multifrequency gold-nanowire antennas. *Phys. Rev. Lett.* **2012**, *108*, 217403.

(14) Kolkowski, R.; Szeszko, J.; Dwir, B.; Kapon, E.; Zyss, J. Effects of surface plasmon polariton-mediated interactions on second harmonic generation from assemblies of pyramidal metallic nanocavities. *Opt. Express* **2014**, *22*, 30592−30606.

(15) Argyropoulos, C.; Ciracì, C.; Smith, D. R. Enhanced optical bistability with film-coupled plasmonic nanocubes. *Appl. Phys. Lett.* **2014**, *104*, 063108.

(16) Lassiter, J. B.; Chen, X.; Liu, X.; Ciracì, C.; Hoang, T. B.; Larouche, S.; Oh, S.-H.; Mikkelsen, M. H.; Smith, D. R. Third-

harmonic generation enhancement by film-coupled plasmonic stripe resonators. *ACS Photonics* **2014**, *1*, 1212−1217.
(17) Huang, Z.; Baron, A.; Larouche, S.; Argyropoulos, C.; Smith, D. R. Optical bistability with film-coupled metasurfaces. *Opt. Lett.* **2015**, *40*, 5638−5641.
(18) Kravtsov, V.; Ulbricht, R.; Atkin, J. M.; Raschke, M. B. Plasmonic nanofocused four-wave mixing for femtosecond near-field imaging. *Nat. Nanotechnol.* **2016**, *11*, 459−464.
(19) Dass, C. K.; Kwon, H.; Vangala, S.; Smith, E. M.; Cleary, J. W.; Guo, J.; Alu, A.; Hendrickson, J. R. Gap-Plasmon-Enhanced Second-Harmonic Generation in Epsilon-Near-Zero Nanolayers. *ACS Photonics* **2020**, *7*, 174−179.
(20) Deng, J.; Tang, Y.; Chen, S.; Li, K.; Zayats, A. V.; Li, G. Giant enhancement of second-order nonlinearity of epsilon-near-zero medium by a plasmonic metasurface. *Nano Lett.* **2020**, *20*, 5421−5427.
(21) Fan, W.; Zhang, S.; Malloy, K.; Brueck, S.; Panoiu, N.; Osgood, R. Second harmonic generation from patterned GaAs inside a subwavelength metallic hole array. *Opt. Express* **2006**, *14*, 9570−9575.
(22) Barrelet, C. J.; Ee, H.-S.; Kwon, S.-H.; Park, H.-G. Nonlinear mixing in nanowire subwavelength waveguides. *Nano Lett.* **2011**, *11*, 3022−3025.
(23) Barakat, E.; Bernal, M.-P.; Baida, F. I. Theoretical analysis of enhanced nonlinear conversion from metallo-dielectric nano-structures. *Opt. Express* **2012**, *20*, 16258−16268.
(24) Aouani, H.; Rahmani, M.; Navarro-Cía, M.; Maier, S. A. Third-harmonic-upconversion enhancement from a single semiconductor nanoparticle coupled to a plasmonic antenna. *Nat. Nanotechnol.* **2014**, *9*, 290−294.
(25) Lehr, D.; Reinhold, J.; Thiele, I.; Hartung, H.; Dietrich, K.; Menzel, C.; Pertsch, T.; Kley, E.-B.; Tü nnermann, A. Enhancing second harmonic generation in gold nanoring resonators filled with lithium niobate. *Nano Lett.* **2015**, *15*, 1025−1030.
(26) Hentschel, M.; Metzger, B.; Knabe, B.; Buse, K.; Giessen, H. Linear and nonlinear optical properties of hybrid metallic−dielectric plasmonic nanoantennas. *Beilstein J. Nanotechnol.* **2016**, *7*, 111−120.
(27) Linnenbank, H.; Grynko, Y.; Förstner, J.; Linden, S. Second harmonic generation spectroscopy on hybrid plasmonic/dielectric nanoantennas. *Light: Sci. Appl.* **2016**, *5*, 16013−16013.
(28) Shibanuma, T.; Grinblat, G.; Albella, P.; Maier, S. A. Efficient third harmonic generation from metal-dielectric hybrid nanoantennas. *Nano Lett.* **2017**, *17*, 2647−2651.
(29) Nielsen, M. P.; Shi, X.; Dichtl, P.; Maier, S. A.; Oulton, R. F. Giant nonlinear response at a plasmonic nanofocus drives efficient four-wave mixing. *Science* **2017**, *358*, 1179−1181.
(30) Wang, F.; Martinson, A. B.; Harutyunyan, H. Efficient nonlinear metasurface based on nonplanar plasmonic nanocavities. *ACS Photonics* **2017**, *4*, 1188−1194.
(31) Wang, F.; Manjare, M.; Lemasters, R.; Li, C.; Harutyunyan, H. Enhancing second-harmonic generation using dipolar-parity modes in non-planar plasmonic nanocavities. *Opt. Lett.* **2019**, *44*, 2787−2790.
(32) Qin, J.; Huang, F.; Li, X.; Deng, L.; Kang, T.; Markov, A.; Yue, F.; Chen, Y; Wen, X.; Liu, S.; Xiong, Q.; Semin, S.; Rasing, T.; Modotto, D.; Morandotti, R.; Xu, J.; Duan, H.; Bi, L. Enhanced Second Harmonic Generation from Ferroelectric HfO_2-Based Hybrid Metasurfaces. *ACS Nano* **2019**, *13*, 1213−1222.
(33) Shen, Q.; Jin, W.; Yang, G.; Rodriguez, A. W.; Mikkelsen, M. H. Active control of multiple, simultaneous nonlinear optical processes in plasmonic nanogap cavities. *ACS Photonics* **2020**, *7*, 901−907.
(34) Deka, G.; Sun, C.-K.; Fujita, K.; Chu, S.-W. Nonlinear plasmonic imaging techniques and their biological applications. *Nanophotonics* **2017**, *6*, 31−49.
(35) Caspani, L.; Xiong, C.; Eggleton, B. J.; Bajoni, D.; Liscidini, M.; Galli, M.; Morandotti, R.; Moss, D. J. Integrated sources of photon quantum states based on nonlinear optics. *Light: Sci. Appl.* **2017**, *6*, 17100−17100.
(36) Celebrano, M.; Wu, X.; Baselli, M.; Großmann, S.; Biagioni, P.; Locatelli, A.; De Angelis, C.; Cerullo, G.; Osellame, R.; Hecht, B.; Duò, L.; Ciccacci, F.; Finazzi, M. Mode matching in multiresonant plasmonic nanoantennas for enhanced second harmonic generation. *Nat. Nanotechnol.* **2015**, *10*, 412−417.
(37) Thyagarajan, K.; Rivier, S.; Lovera, A.; Martin, O. J. Enhanced second-harmonic generation from double resonant plasmonic antennae. *Opt. Express* **2012**, *20*, 12860−12865.
(38) Aouani, H.; Navarro-Cia, M.; Rahmani, M.; Sidiropoulos, T. P.; Hong, M.; Oulton, R. F.; Maier, S. A. Multiresonant broadband optical antennas as efficient tunable nanosources of second harmonic light. *Nano Lett.* **2012**, *12*, 4997−5002.
(39) De Luca, F.; Ciracì, C. Difference-frequency generation in plasmonic nanostructures: a parameter-free hydrodynamic description. *J. Opt. Soc. Am. B* **2019**, *36*, 1979−1986.
(40) Butet, J.; Brevet, P.-F.; Martin, O. J. Optical second harmonic generation in plasmonic nanostructures: from fundamental principles to advanced applications. *ACS Nano* **2015**, *9*, 10545−10562.
(41) Kauranen, M.; Zayats, A. V. Nonlinear plasmonics. *Nat. Photonics* **2012**, *6*, 737−748.
(42) Echarri, A. R.; Cox, J. D.; Yu, R.; Garcia de Abajo, F. J. Enhancement of nonlinear optical phenomena by localized resonances. *ACS Photonics* **2018**, *5*, 1521−1527.
(43) Czaplicki, R.; Husu, H.; Siikanen, R.; Mäkitalo, J.; Kauranen, M.; Laukkanen, J.; Lehtolahti, J.; Kuittinen, M. Enhancement of second-harmonic generation from metal nanoparticles by passive elements. *Phys. Rev. Lett.* **2013**, *110*, 093902.
(44) Wells, B.; Bykov, A. Y.; Marino, G.; Nasir, M. E.; Zayats, A. V.; Podolskiy, V. A. Structural second-order nonlinearity in plasmonic metamaterials. *Optica* **2018**, *5*, 1502−1507.
(45) Czaplicki, R.; Kiviniemi, A.; Huttunen, M. J.; Zang, X.; Stolt, T.; Vartiainen, I.; Butet, J.; Kuittinen, M.; Martin, O. J.; Kauranen, M. Less is more: Enhancement of second-harmonic generation from metasurfaces by reduced nanoparticle density. *Nano Lett.* **2018**, *18*, 7709−7714.
(46) Scalora, M.; Vincenti, M.; de Ceglia, D.; Akozbek, N.; Bloemer, M.; De Angelis, C.; Haus, J.; Vilaseca, R.; Trull, J.; Cojocaru, C. Harmonic generation from metal-oxide and metal-metal boundaries. *Phys. Rev. A: At., Mol., Opt. Phys.* **2018**, *98*, 023837.
(47) Holland, W. R.; Hall, D. G. Frequency Shifts of an Electric-Dipole Resonance near a Conducting Surface. *Phys. Rev. Lett.* **1984**, *52*, 1041−1044.
(48) Aubry, A.; Lei, D. Y.; Maier, S. A.; Pendry, J. B. Plasmonic hybridization between nanowires and a metallic surface: a transformation optics approach. *ACS Nano* **2011**, *5*, 3293−3308.
(49) Lévêque, G.; Martin, O. J. Optical interactions in a plasmonic particle coupled to a metallic film. *Opt. Express* **2006**, *14*, 9971−9981.
(50) Mock, J. J.; Hill, R. T.; Degiron, A.; Zauscher, S.; Chilkoti, A.; Smith, D. R. Distance-dependent plasmon resonant coupling between a gold nanoparticle and gold film. *Nano Lett.* **2008**, *8*, 2245−2252.
(51) Ciracì, C.; Hill, R. T.; Mock, J. J.; Urzhumov, Y.; Fernández-Domínguez, A. I.; Maier, S. A.; Pendry, J. B.; Chilkoti, A.; Smith, D. R. Probing the ultimate limits of plasmonic enhancement. *Science* **2012**, *337*, 1072−1074.
(52) Moreau, A.; Ciracì, C.; Mock, J. J.; Hill, R. T.; Wang, Q.; Wiley, B. J.; Chilkoti, A.; Smith, D. R. Controlled-reflectance surfaces with film-coupled colloidal nanoantennas. *Nature* **2012**, *492*, 86−89.
(53) Hao, J.; Wang, J.; Liu, X.; Padilla, W. J.; Zhou, L.; Qiu, M. High performance optical absorber based on a plasmonic metamaterial. *Appl. Phys. Lett.* **2010**, *96*, 251104.
(54) Ciracì, C.; Chen, X.; Mock, J. J.; McGuire, F.; Liu, X.; Oh, S.-H.; Smith, D. R. Film-coupled nanoparticles by atomic layer deposition: Comparison with organic spacing layers. *Appl. Phys. Lett.* **2014**, *104*, 023109.
(55) Lassiter, J. B.; McGuire, F.; Mock, J. J.; Ciracì, C.; Hill, R. T.; Wiley, B. J.; Chilkoti, A.; Smith, D. R. Plasmonic waveguide modes of film-coupled metallic nanocubes. *Nano Lett.* **2013**, *13*, 5866−5872.
(56) Knebl, D.; Hörl, A.; Trügler, A.; Kern, J.; Krenn, J. R.; Puschnig, P.; Hohenester, U. Gap plasmonics of silver nanocube dimers. *Phys. Rev. B: Condens. Matter Mater. Phys.* **2016**, *93*, 081405.
(57) Rose, A.; Hoang, T. B.; McGuire, F.; Mock, J. J.; Ciracì, C.; Smith, D. R.; Mikkelsen, M. H. Control of radiative processes using

https://dx.doi.org/10.1021/acsphotonics.0c01545
ACS Photonics 2020, 7, 3333−3340

tunable plasmonic nanopatch antennas. *Nano Lett.* **2014**, *14*, 4797−4802.
(58) Ciracì, C.; Lassiter, J. B.; Moreau, A.; Smith, D. R. Quasi-analytic study of scattering from optical plasmonic patch antennas. *J. Appl. Phys.* **2013**, *114*, 163108.
(59) Akselrod, G. M.; Ming, T.; Argyropoulos, C.; Hoang, T. B.; Lin, Y.; Ling, X.; Smith, D. R.; Kong, J.; Mikkelsen, M. H. Leveraging Nanocavity Harmonics for Control of Optical Processes in 2D Semiconductors. *Nano Lett.* **2015**, *15*, 3578−3584.
(60) Metzger, B.; Gui, L.; Fuchs, J.; Floess, D.; Hentschel, M.; Giessen, H. Strong enhancement of second harmonic emission by plasmonic resonances at the second harmonic wavelength. *Nano Lett.* **2015**, *15*, 3917−3922.
(61) Guddala, S.; Ramakrishna, S. A. Optical limiting by nonlinear tuning of resonance in metamaterial absorbers. *Opt. Lett.* **2016**, *41*, 5150−4.
(62) Liu, X.; Larouche, S.; Bowen, P.; Smith, D. R. Clarifying the origin of third-harmonic generation from film-coupled nanostripes. *Opt. Express* **2015**, *23*, 19565−19574.
(63) Butet, J.; Dutta-Gupta, S.; Martin, O. J. F. Surface second-harmonic generation from coupled spherical plasmonic nanoparticles: Eigenmode analysis and symmetry properties. *Phys. Rev. B: Condens. Matter Mater. Phys.* **2014**, *89*, 245449−10.
(64) Zeng, Y.; Qian, H.; Rozin, M. J.; Liu, Z.; Tao, A. R. Enhanced Second Harmonic Generation in Double-Resonance Colloidal Metasurfaces. *Adv. Funct. Mater.* **2018**, *28*, 1803019−8.
(65) Dicken, M. J.; Sweatlock, L. A.; Pacifici, D.; Lezec, H. J.; Bhattacharya, K.; Atwater, H. A. Electrooptic modulation in thin film barium titanate plasmonic interferometers. *Nano Lett.* **2008**, *8*, 4048−4052.
(66) Müller, J.; Schröder, U.; Böscke, T.; Müller, I.; Böttger, U.; Wilde, L.; Sundqvist, J.; Lemberger, M.; Kücher, P.; Mikolajick, T.; Frey, L. Ferroelectricity in yttrium-doped hafnium oxide. *J. Appl. Phys.* **2011**, *110*, 114113.
(67) Olmon, R. L.; Slovick, B.; Johnson, T. W.; Shelton, D.; Oh, S.-H.; Boreman, G. D.; Raschke, M. B. Optical dielectric function of gold. *Phys. Rev. B: Condens. Matter Mater. Phys.* **2012**, *86*, 235147.

https://dx.doi.org/10.1021/acsphotonics.0c01545
ACS Photonics 2020, 7, 3333−3340